

## Self-assembly of magnetic Co atoms on stanene

Nitin Kumar <sup>1,\*</sup>, Ye-Shun Lan,<sup>1,\*</sup> Chia-Ju Chen <sup>1</sup>, Yen-Hui Lin,<sup>1</sup> Shih-Tang Huang,<sup>1</sup>  
Horng-Tay Jeng,<sup>1,2,3,4,†</sup> and Pin-Jui Hsu <sup>1,2,‡</sup>

<sup>1</sup>*Department of Physics, National Tsing Hua University, Hsinchu 300044, Taiwan*

<sup>2</sup>*Center for Quantum Technology, National Tsing Hua University, Hsinchu 300044, Taiwan*

<sup>3</sup>*Physics Division, National Center for Theoretical Sciences, Hsinchu 300044, Taiwan*

<sup>4</sup>*Institute of Physics, Academia Sinica, Taipei 11529, Taiwan*



(Received 26 January 2022; revised 28 April 2022; accepted 17 May 2022; published 1 June 2022)

We have investigated magnetic Co atoms self-assembled on ultraflat stanene on Cu(111) substrate by utilizing scanning tunneling microscopy/spectroscopy (STM/STS) in conjunction with density functional theory (DFT). By means of depositing Co onto the stanene/Cu(111) held at 80 K, Co atoms have developed into monomer, dimer, and trimer structures containing one, two, and three Co atoms, respectively. As per atomically resolved topographic images and bias-dependent apparent heights, the atomic structure models based on Sn atoms substituted by Co atoms have been deduced, which are in agreement with both self-consistent DFT calculations and STM simulations. Apart from that, the projected density of states has revealed a maximum at around  $-0.5$  eV from the Co- $3d_{3z^2-r^2}$  minority band, which contributes predominately to the peak feature at about  $-0.3$  eV in tunneling conductance ( $dI/dU$ ) spectra taken at the Co atomic sites. As a result of the exchange splitting between the Co- $3d$  majority and minority bands, there are nonzero magnetic moments, including about  $0.60\mu_B$  in monomer,  $0.56\mu_B$  in dimer, and  $0.29\mu_B$  in trimer of the Co-atom assembly on the stanene. Such a magnetic Co-atom assembly, therefore, could provide the vital building blocks to stabilize the local magnetism on two-dimensional stanene with nontrivial topological properties.

DOI: [10.1103/PhysRevMaterials.6.066001](https://doi.org/10.1103/PhysRevMaterials.6.066001)

### I. INTRODUCTION

Topological phases of matter have been at the center of active research since their theoretical discovery back in 1972 [1–5]. Topological materials provide an ideal platform for the study of fundamental physical phenomena [6–8] and the development of technical applications such as quantum computing [9,10], spintronics [11], and low-power electronics. Topological insulators (TIs) [5,12–19] are one of the important topological quantum materials in condensed-matter physics, and they have topologically protected gapless states on the surface/edge in addition to the bulk band gap [3,20]. Gapless edge states provide dissipationless conducting channels as they are immune to the electron backscattering by nonmagnetic defects [15] and disorders [21]. In the presence of an external magnetic field, the induced energy quantization of Landau levels gives rise to the quantum Hall effect (QHE), resulting in the quantization of the Hall conductance in units of  $e^2/h$  (where  $e$  is the electronic charge, and  $h$  is Planck's constant) [6,7].

Low temperature and the presence of a strong external magnetic field are required to accomplish Hall quantization in a quantum Hall insulator (QHI) [22], which limits their usage in practical applications. The Haldane model [23] proposed

the spin version of the QHE referred to as the quantum spin Hall effect (QSHE) [8,23–27] in a two-dimensional (2D) honeycomb lattice having an alternating intrinsic magnetic field of zero net flux. Kane and Mele presented spin-orbit coupling (SOC) in graphene as an intrinsic magnetic field [24], and they established graphene as the first realistic quantum spin Hall insulator (QSHI); the QSHIs are time-reversal invariant, and the corresponding topology in electronic structures is mainly driven by a combination of SOC and time-reversal symmetry [3]. However, due to the weak SOC, the pristine bulk energy gap in graphene is too small (of the order of  $10^{-3}$  meV) to measure directly in experiments [28]. On the contrary, 2D honeycomb stanene, which is the tin (Sn) counterpart of graphene, ended the search for a sizable bulk band gapped TI with an inverted gap of 300 meV [29,30], and it became an ideal choice for the study of QSHE.

Another quantum phenomenon called the quantum anomalous Hall effect (QAHE) [31–37] also has a dissipationless conducting edge feature similar to the QHE without the external magnetic field and the quantization of Landau levels [38–40]. Unlike the QSHE, the QAHE originates from the breaking of time-reversal symmetry as a result of the presence of an intrinsic magnetic ordering [41]. In magnetic TIs (or quantum anomalous Hall insulators), intrinsic magnetization combined with SOC drives the exchange gap accompanied by chiral edge modes, which provide the dissipationless conducting channels [42]. Recently, several successful attempts to realize the QAHE in 3D TIs by stabilizing a long-range magnetic ordering were reported. The magnetic bulk compound

\*These authors contributed equally to this work.

†jeng@phys.nthu.edu.tw

‡pinjuis@phys.nthu.edu.tw

materials, such as Cr-doped  $(\text{Bi}_x\text{Sb}_{1-x})_2\text{Te}_3$  [31,32], V-doped  $(\text{Bi,Sb})_2\text{Te}_3$  [43,44],  $\text{MnBi}_2\text{Te}_4$  [36,45], and  $\text{MnBi}_2\text{Te}_7$  [46], are a few examples where the QAHE naturally occurs. Since the TIs of the  $\text{Bi}_2\text{Se}_3$  family have a simple surface Dirac cone structure with a large bulk band gap up to 0.3 eV [47,48], the adjacent ferromagnetic layers in  $(\text{Bi}_2\text{Te}_3)_n(\text{MnBi}_2\text{Te}_4)$  couple in an antiparallel manner and exhibit the antiferromagnetic spin texture in bulk form, and they demonstrate the QAHE only with an odd number of layers [36,49,50].

Recently, in order to realize the QAHE down to the 2D limit, ultrathin film TIs with atomic thickness have received much attention. Since the QSHE can be considered as two copies of the QAHE with magnetization vectors in opposite directions, the existence of magnetization further drives one copy to the topological trivial phase and leaves another one in the nontrivial topological phase, which transforms a non-magnetic TI into a magnetic TI [31,32,36,51]. Based on this mechanism, introducing magnetism to atomic-thick topological materials becomes an important issue, and it is worth the effort to carry out studies down to the atomic scale.

In this present work, we have successfully fabricated the magnetic Co-atom assembly on ultraflat stanene on Cu(111) substrate held at 80 K. We have investigated the surface structures and electronic properties by using scanning tunneling microscopy/spectroscopy (STM/STS) combined with density functional theory (DFT). In the dilute limit of coverage, Co atoms have replaced Sn atoms and developed into the monomer, dimer, and trimer structures on the stanene. Furthermore, the atomic structure models for magnetic Co assembly have been deduced based on the bias-dependent atomic resolution images and apparent heights, which are in line with the self-consistent lattice relaxations in DFT as well as the topographic images and line profiles in STM simulations. In addition, the tunneling  $dI/dU$  spectra have resolved a conductance peak at about  $-0.3$  eV on the Co atomic sites, which is mainly dominated by the maximum of the projected density of states (PDOS) at around  $-0.5$  eV from the Co- $3d_{3z^2-r^2}$  minority band. Due to the exchange-split majority and minority Co- $3d$  bands, the net magnetic moments, i.e., about  $0.60\mu_B$  in monomer,  $0.56\mu_B$  in dimer, and  $0.29\mu_B$  in trimer, remain present in the Co atomic structures. Given the magnetic keystones constructed by the atomic-scale Co assembly, the local magnetism thus has an opportunity to be stabilized on the 2D topological nontrivial stanene.

## II. EXPERIMENTAL AND THEORETICAL METHODS

### A. Experimental details

The whole experiment was performed in an ultrahigh vacuum (UHV) environment of order  $10^{-10}$  mbar. The Cu(111) substrate was cleaned by several cycles of  $\text{Ar}^+$  sputtering and annealing. High-purity tin (Sn) (99.99%) was evaporated from a PBN crucible in an e-beam evaporator (FOCUS) while keeping the substrate at a low temperature ( $T \approx 80$  K). Deposition of Sn was followed by the evaporation of cobalt (Co) atoms by heating a Co-wire (99.99%) in an e-beam evaporator (FOCUS-EFM3). After the preparation, the sample was transferred to the measurement chamber, where a low-temperature scanning tunneling microscope (LT-STM) (UNISOKU,

USM-1500), with a base temperature of 4.2 K, was employed to characterize it. All topographic images were scanned in constant current mode and *in situ* tunneling conductance ( $dI/dU$ ) spectra, and maps were recorded with the help of an external lock-in amplifier (Stanford Research Systems) at a frequency of 3991 Hz and 20–50 mV voltage modulation.

### B. Theoretical computations

First-principles calculations were performed using the Vienna Ab Initio Simulation Package (VASP) based on density functional theory (DFT). The generalized gradient approximation (GGA) in the Perdew-Burke-Ernzerhof (PBE) [52–54] form was used for exchange-correlation potential in the projector augmented wave (PAW) pseudopotential [55]. A plane-wave cutoff energy of 273 eV was adopted in the slab model calculations with a vacuum layer thickness of 25 Å well separating the slabs. A single-layer  $2 \times 2$  supercell of stanene on top of a seven-layer  $4 \times 4$  supercell of Cu(111) was used for the Co-monomer model, while monolayer  $3 \times 3$  stanene/seven-layer  $6 \times 6$  Cu(111) was used for the Co-dimer and Co-trimer models. Then we properly replaced the Sn atoms with the Co atoms and carried out geometry optimization of the large superstructure using the  $\Gamma$  point for the  $k$ -space until the total energy and the residual atomic force were converged within  $10^{-4}$  eV and  $-0.005$  eV/Å, respectively. The self-consistent calculations of the relaxed lattice structure were performed using a  $6 \times 6 \times 1$  Monkhorst-Pack  $k$ -grid mesh with the spin-orbit coupling (SOC) included.

## III. RESULTS AND DISCUSSION

The ultraflat stanene was prepared following a procedure analogous to that described in work done by Deng *et al.* [30], the clean Cu(111) substrate was first cooled down to 80 K on a cooling manipulator, and then Sn was evaporated from a thermal evaporator. The flat 2D stanene grown in uniform and large sized islands on Cu(111) was characterized by a low-temperature STM (LT-STM) at 4.2 K. Figure 1(a) shows an overview of 2D stanene islands, where about two-thirds of the Cu(111) substrate surface has been covered. The step height of the 2D stanene island was measured as  $0.166 \pm 0.02$  nm [see the top panel in Fig. 1(c)] from the topographic line profile along the black arrow line in Fig. 1(a). Six Sn atoms in the honeycomb structure can be clearly seen in Fig. 1(b), which shows an atomic resolution image. The Sn-Sn bond length was measured to be 0.31 nm from the topographic line profile in Fig. 1(c) (bottom panel) taken along the green arrow in Fig. 1(b), which is close to the bond length in free-standing stanene (0.28 nm) [29]. The topographic line profile in Fig. 1(c) (bottom panel) also demonstrates that the height of all Sn atoms is equivalent, which confirms the flatness of the stanene. The lattice constant of honeycomb stanene was measured to be 0.51 nm, which is in line with the double of Cu(111) lattice constant (0.255 nm). The honeycomb unit cell is marked with red arrow lines in Fig. 1(b) and a red rhombus in Fig. 1(d), which comprises two Sn atoms absorbed on a  $2 \times 2$  Cu(111) supercell and situated on hcp and fcc hollow sites. The structure model for honeycomb stanene has been

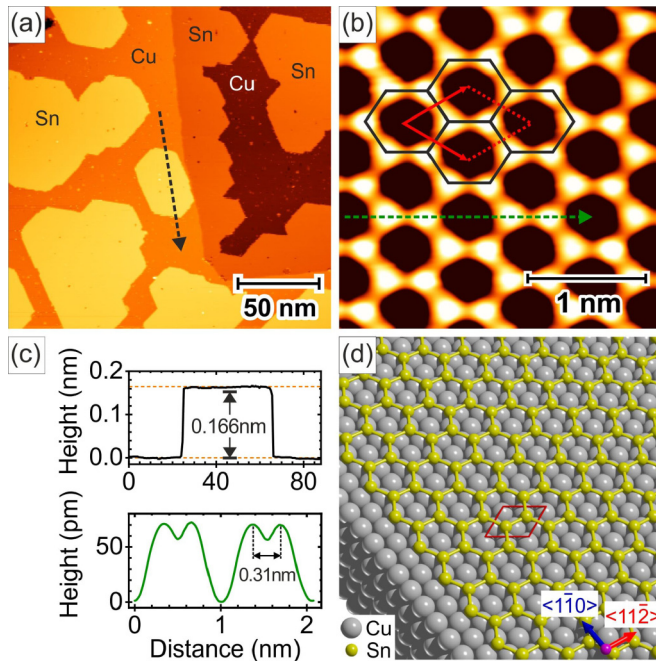


FIG. 1. Ultraflat stanene on Cu(111). (a) An overview STM image of 2D islands of stanene on Cu(111) substrate. (b) Zoom-in image of one stanene island showing the flat honeycomb structure. The unit cell of stanene with the lattice constant of 0.51 nm is marked by red arrow lines. (c) Line profiles along the black and green dotted arrows in (a) and (b), respectively, showing that the height of the stanene island is 0.16 nm and the Sn-Sn bond length is 0.31 nm. (d) Structure model of flat honeycomb stanene on Cu(111) substrate. Gray and green balls represent the Cu and Sn atoms, respectively. [Scan parameters for (a)  $V_s = 200$  mV,  $I_s = 400$  pA; (b)  $V_s = 200$  mV,  $I_s = 1$  nA.]

shown in Fig. 1(d) with a termination at the zigzag edge as reported before [30].

As was reported, the flat stanene is a time-reversal invariant topological material with a large SOC gap [29,30]. To introduce the magnetism to the topological nontrivial stanene, we have deposited the Co atoms onto the 2D stanene islands/Cu(111). The Co atoms were evaporated at a substrate temperature of 80 K, and the corresponding overview STM image has been shown in Fig. 2(a), where many bright protrusions, small black holes, and the irregular edges can be seen on the 2D stanene island after the Co deposition. According to the zoom-in image shown in Fig. 2(b) taken at the area marked by a black squared frame in Fig. 2(a), there are self-assembled Co atomic structures consisting of one, two, and three bright protrusions as circled by green, magenta, and blue colors, respectively. In contrast to Fig. 2(b), which was taken at a negative bias voltage (filled state), Fig. 2(c) represents the topographic image taken at a positive bias voltage (empty state) of the same scanning spot, and the Co-atom assembly appears differently in morphology. The bias-dependent topographic line profiles for the Co-atom assembly (green, magenta, and blue arrow lines) measured at the filled [Fig. 2(b)] as well as the empty [Fig. 2(c)] states have been arranged in Fig. 2(d) for a direct comparison.

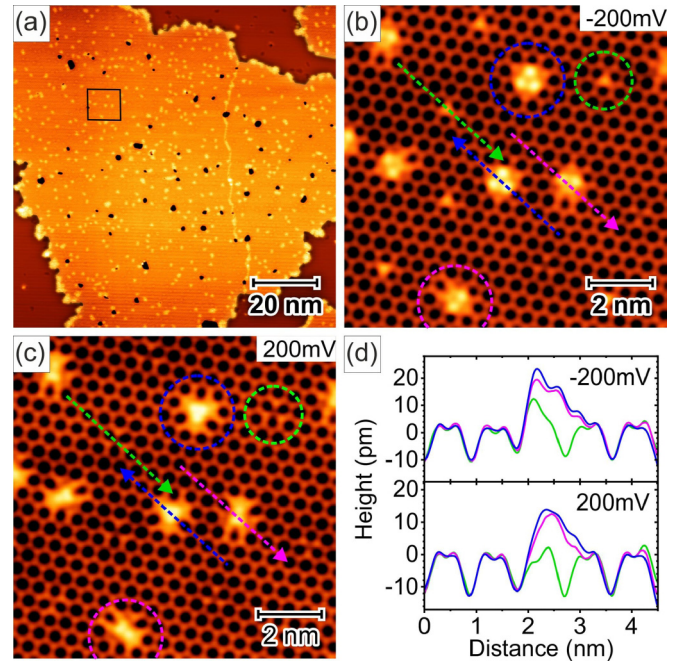


FIG. 2. Self-assembled Co atomic structures on honeycomb stanene. (a) An overview STM image of stanene island after a cold deposition of Co atoms. (b) Zoom-in STM image of the black squared area in (a) taken at the negative bias voltage (filled state). The self-assembled Co atomic structures consisting of one, two, and three bright protrusions have been marked by green, magenta, and blue circles, respectively. (c) Zoom-in STM image of the same location with (b) taken at the positive bias voltage (empty state), where the Co-atom assembly appears differently in morphology. (d) Bias-dependent topographic line profiles along the green, magenta, and blue arrow lines in (b) and (c). [Scan parameters for (a)  $V_s = 1$  V,  $I_s = 400$  pA; (b)  $V_s = -200$  mV,  $I_s = 1$  nA; and (c)  $V_s = +200$  mV,  $I_s = 1$  nA.]

### A. Monomer

Starting with a single bright protrusion (green circle) of three different Co atomic structures observed in Fig. 2(b), the energetic and hot Co atom coming from the evaporator may be able to substitute one Sn atom from either the hcp-hollow or the fcc-hollow site of the Cu(111) surface. According to the adsorption position and apparent height in the atomic resolution image of Fig. 2(b), the resultant proposed atomic structure model for the Co monomer that consists of replacing one Sn atom with one Co atom in stanene has been shown in Fig. 3(a). The topographic appearance of the Co monomer appears as a bright protrusion in the filled state (negative sample bias) but looks like a dip in the empty state (positive sample bias) [see Figs. 3(b) and 3(d)]. The DFT calculations on self-consistent lattice relaxations show that the Co atom is located 0.51 Å lower than that of stanene. However, the apparent height of the Co monomer in STM images under negative bias is around 0.1 Å higher than that of stanene. This is due to the much higher density of states (DOS) of the Co-3d band right below the Fermi level ( $E_F$ ) with respect to the lower DOS of Sn, as shown in Figs. 7(a) and 7(b), giving rise to higher charge density and tunneling current for the filled states. Consequently, the apparent height of Co imaged at

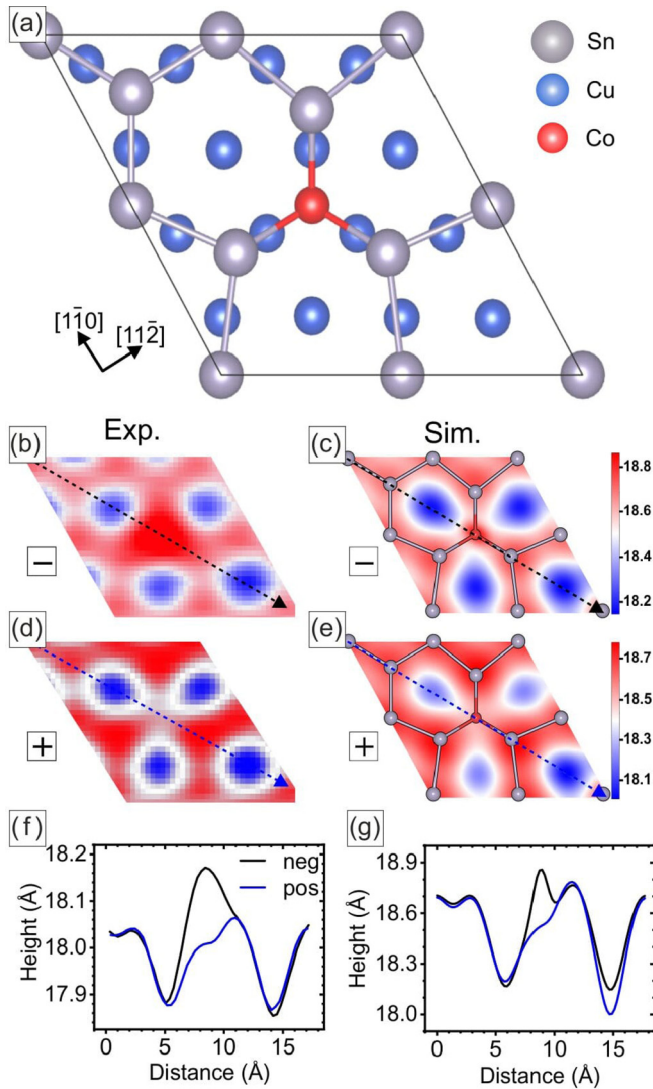


FIG. 3. Co monomer. (a) Proposed structure model for Co monomer from substituting one Sn atom for a Co atom in the honeycomb stanene on Cu(111) substrate. Gray, blue, and red balls in the model represent Sn, Cu, and Co atoms, respectively. (b), (d) Atomically resolved experimental STM images of Co monomer in negative and positive sample biases. Red (blue) indicates high (low) magnitude. (c), (e) Simulated STM images based on the structure model in (a) showing an agreement with the experimental results. (f), (g) Bias-dependent line profiles along the black and blue dashed lines in (b)–(e).

negative sample bias in STM topography [Fig. 3(b)] is constantly higher than that of Sn, even though the position of Co is lower than Sn. This interesting phenomenon is further supported by the STM image simulations as shown in Figs. 3(c) and 3(e), which agree well with the experimental STM images in Figs. 3(b) and 3(d). We denote that the total free energy of Co monomer on an fcc-hollow site is about 95 meV lower than on an hcp-hollow site, therefore the fcc-hollow site is more energetically preferred.

To further quantify the apparent height of the Co monomer on the stanene, we have presented the experimental and theoretical line cuts (black and blue dashed lines) along the

diagonal direction of the supercell under negative and positive bias voltages as shown in Figs. 3(f) and 3(g), respectively. Five features can be found through this line, which correspond individually to the heights from Sn, Sn, Co, Sn, and Sn atoms (left to right), where they behave differently in heights for different bias voltages. It can be seen that under negative bias voltage, the Co peak is significantly higher than the Sn peak, whereas the order reverses under the positive bias voltage. Both the experimental and the theoretical height profiles agree fairly well with each other.

### B. Trimer

After the Co monomer, it is easier to discuss the high-symmetric Co atomic structure with three bright protrusions (blue circle) than the low-symmetric Co atomic structure with two bright protrusions (magenta circle), as shown in Fig. 2(b). The threefold symmetric Co atomic structure model has been constructed in two steps: First, four adjacent Sn atoms were replaced by four Co atoms, forming a big Co triangle. Second, the central Co atom was replaced by a small Sn triangle as shown in Fig. 4(a), and we assign this structure as the Co trimer in the following (see Fig. S1 in the Supplemental Material [56] for details). Note that the substitution of Sn atoms by Co atoms is analogous to the known doping process of semiconductors, the atomic lattice structure of stanene has been locally changed, and the number of Sn atoms does not need to be conserved. Because they are of the same element, the hot Co atoms with enough kinetic energy tend to self-nucleate, as one might expect. Unlike monomers, dimers and trimers were likely formed when two and three Co atoms had nucleated first and then substituted Sn atoms. Similar to the monomer case, not only were the structural relaxations of Co trimer carried out, but also its PDOS was calculated, as shown in Fig. 7(d), showing that the Co-3*d* band dominates below  $E_F$  (filled states). The resultant bias-dependent simulated STM images are shown in Figs. 4(c) and 4(e). In the filled-state STM images [Figs. 4(b) and 4(c)], the topography of the trimer structure appears as an upside-down triangle driven from the three Co atoms. In the empty-state STM images [Figs. 4(d) and 4(e)], the topography of the trimer structure appears as a triangle of comparably smaller size, driven from the three middle Sn atoms. Note that not only are the simulated STM images in good agreement with the experimental STM images [Figs. 4(b) and 4(d)], but also the corresponding height profiles are reasonably consistent with each other [Figs. 4(f) and 4(g)]. We note that different structure models have also been proposed for Co trimer, but they are not stable, nor do they reproduce experimental results (see Fig. S2 of the Supplemental Material [56] for details).

### C. Dimer

The structure model of the low-symmetric Co atomic structure with two bright protrusions (magenta circle) shown in Fig. 2(b) has been deduced from the high-symmetric Co trimer structure model in Fig. 4(a) (see Fig. S1 of the Supplemental Material [56] for details). One Co atom has been removed from the Co trimer structure in Fig. 4(a), and the corresponding Co dimer structure is shown in Fig. 5(a). In

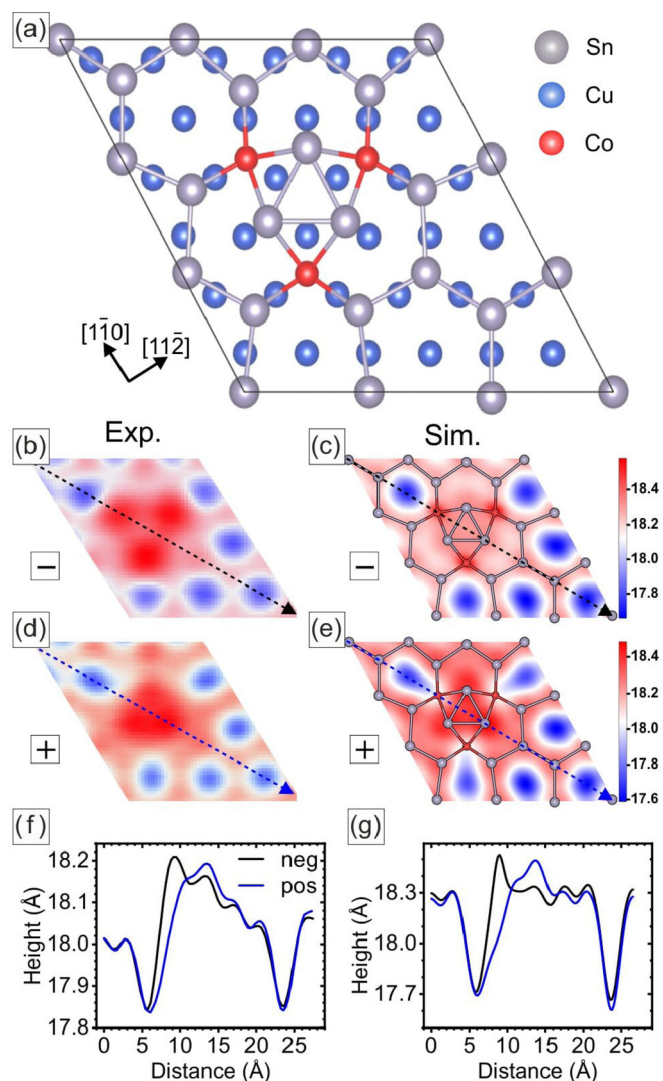


FIG. 4. Co trimer. (a) Proposed structure model for Co trimer. Three Co atoms have substituted three Sn atoms in the stanene and form an upside-down triangle. Gray, blue, and red balls represent Sn, Cu, and Co atoms, respectively. (b), (d) Atomically resolved experimental STM images of Co trimer in negative and positive sample biases. Red (blue) indicates high (low) magnitude. (c), (e) Simulated STM images based on the structure model in (a) are consistent with the topographic features and symmetry observed in the experimental STM images. (f), (g) Bias-dependent height profiles along the black and blue dashed lines in (b)–(e).

this model, two Co atoms substitute two Sn atoms from the two identical positions in the honeycomb lattice. The PDOS of Co dimer has been calculated in Fig. 7(c) and also shows the prominent contribution of the Co-3d band in the energy range below  $E_F$ . The simulated STM images of the Co dimer structure under different biases show clearly different characters: In the negative bias, a dumbbell-like shape contour emerges from the Co dimer region in Fig. 5(c), whereas in the positive bias a triangle-like contour driven from the central Sn triangle appears in Fig. 5(e). Such bias-dependent simulated STM images support the experimental observations that a dumbbell-like Co dimer is relatively brighter in the

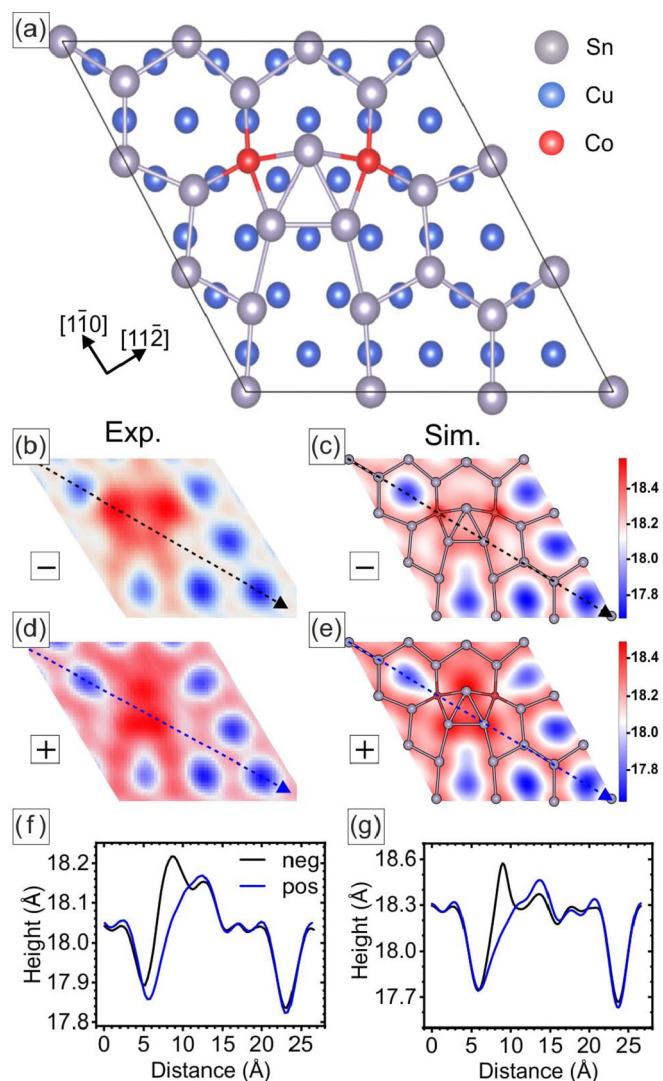


FIG. 5. Co dimer. (a) Proposed structure model for Co dimer. The low-symmetric Co dimer structure has been deduced from modifying the high-symmetric Co trimer structure by removing one substituted Co atom. Gray, blue, and red balls in the model represent Sn, Cu, and Co atoms, respectively. (b), (d) Atomically resolved experimental STM images of Co dimer in negative and positive sample biases. Red (blue) indicates high (low) magnitude. (c), (e) Simulated STM images based on the structure model in (a) representing a good consistency with experimental STM images. (f), (g) Bias-dependent height profiles along the black and blue dashed lines in (b)–(e).

negative bias of Fig. 5(b), but the Sn triangle becomes more pronounced in the positive bias of Fig. 5(d). It is also noted that the bias-dependent height profiles have been further examined, and they are also consistent in both experiments and simulations as shown in Figs. 5(f) and 5(g). Note that there have been other structure models proposed for Co dimer, but they do not agree with either theoretical calculations or experimental observations (see Fig. S3 of the Supplemental Material [56] for details).

Figures 6(a) and 6(c) represent the bias-dependent topographic images taken at the negative (filled state) and the positive biases (empty state), respectively. The corresponding

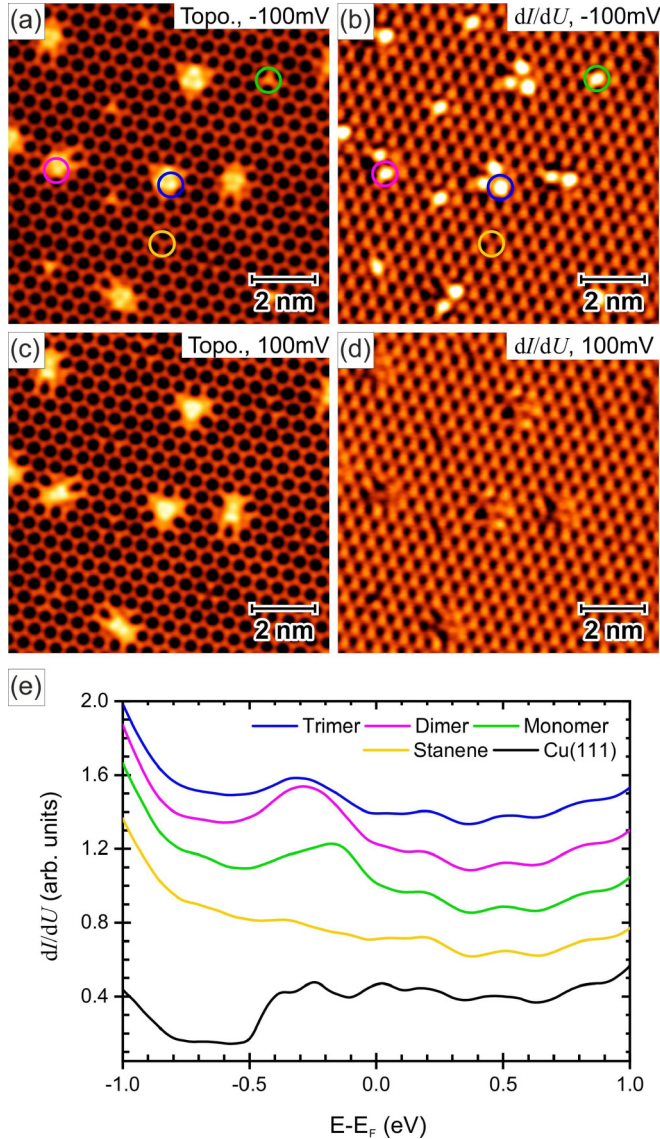
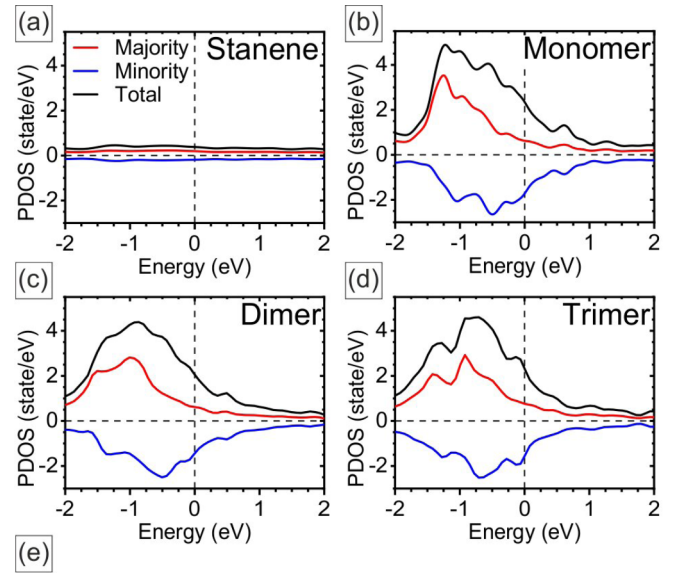


FIG. 6. Bias-dependent  $dI/dU$  maps. (a), (c) Filled- and empty-state STM topographic images of Co-atom assembly on honeycomb stanene. (b), (d)  $dI/dU$  maps corresponding to (a) and (c). (e)  $dI/dU$  curves as a function of sample bias [positions where the  $dI/dU$  curves are taken have been marked with corresponding colored circles in (a) and (b)]. [Scan parameters for (a), (c)  $V_s = -100, +100$  mV,  $I_s = 1$  nA; (b), (d)  $V_s = -100, +100$  mV,  $I_s = 1$  nA; stabilization parameters for (e)  $V_s = +1.0$  V,  $I_s = 1$  nA.]

$dI/dU$  maps of the Co-atom assembly on stanene have been shown in Figs. 6(b) and 6(d), displaying a bias dependence as well. To understand the local density of states (LDOS) of these self-assembled Co atomic structures, we have exploited the STS measurements with high spatial and energy resolution. The systematic studies of  $dI/dU$  curves acquired at the different positions have been arranged in Fig. 6(e). The black line is the  $dI/dU$  curve taken from the bare Cu(111), where the well-known Shockley surface state at  $-0.44$  eV has been resolved. A nearly featureless  $dI/dU$  curve (yellow line) indicates the constant DOS of stanene, which is in line with the PDOS calculated in Fig. 7(a). The  $dI/dU$  spectra measured



System	Magnetic Moment ( $\mu_B$ )		
	Co1	Co2	Co3
Monomer/Stanene/Cu(111)	0.601		
Dimer/Stanene/Cu(111)	0.559	0.559	
Trimer/Stanene/Cu(111)	0.288	0.289	0.293
Co(adatom)/Cu(111) [57]	1.92		
Co(adatom)/Cu(111) [58]	2.06		

FIG. 7. Projected density of states (PDOS) and magnetic moments. (a)–(d) PDOS curves for pristine stanene, Co monomer, dimer, and trimer. (e) Table of calculated magnetic moments of the individual Co atoms in monomer, dimer, and trimer structures on stanene/Cu(111). The magnetic moment of Co adatom on pristine Cu(111) has also been included.

at the Co atomic sites of Co monomer (green circle), dimer (magenta circle), and trimer (blue circle) exhibit a broad peak feature at around  $-0.3$  eV. This peak feature resolved in the  $dI/dU$  spectra is also reflected in the bias-dependent  $dI/dU$  maps as shown in Figs. 6(b) and 6(d), where Co monomer, dimer, and trimer have high conductance intensity and appear bright in the negative bias (filled state), but they have no significant contrast as compared to honeycomb stanene in the positive bias (empty state). In contrast to the filled state topography in which the Co atoms appear as bright dots due to the higher tunneling current, the bright features of dimer and trimer in the empty-state topography are mainly driven from the middle Sn triangles [Figs. 5(a) and 5(d) and Figs. 4(a) and 4(d)], whereas the monomer appears as a dip because of the absence of a Sn triangle [Figs. 3(a) and 3(d)]. Despite being the same element, middle Sn triangles bonding with Co in the dimer and trimer can have more tunneling current than the other Sn atoms in the stanene according to simulated STM images shown in Figs. 4(e) and 5(e). The possible reasons are associated with underlying mechanisms, e.g., hybridization of atomic orbitals, modified bonding geometry, electric charge transfer, etc., which could all have contributions to the LDOS and eventually lead to the bias-dependent topographic images

not only observed experimentally but also reproduced by STM simulations as shown in Figs. 3, 4, and 5.

The PDOS of stanene, Co monomer, Co dimer, and Co trimer have been presented in Fig. 7. The intensity of Sn PDOS is relatively low and featureless in the energy dispersion of  $\pm 2.0$  eV with respect to  $E_F$ . In addition, the PDOS for the Co monomer, Co dimer, and Co trimer have been shown in Figs. 7(b), 7(c) and 7(d), respectively, and their PDOSs clearly show an exchange splitting that originates from the Co-3d majority (red) and minority (blue) bands. By taking the Co monomer as an example, the splitting can be easily identified from a maximum at  $-1.25$  eV of the Co-3d majority spin band (red line) and a maximum at around  $-0.5$  eV of the Co-3d minority spin band (blue line), and the same analogy can be applied for the cases of Co dimer and trimer. Interestingly, we have found that such exchange splitting between the Co-3d majority and minority bands continuously reduces from the Co monomer to the Co trimer, implying the delocalization of  $d$  electrons due to a greater hybridization and orbital overlapping with Sn atoms in the Co-dimer and -trimer configurations. Given the exchange-split Co-3d majority and minority bands, the net magnetic moments of the Co-atom assembly on the stanene have been evaluated and they are nearly  $0.60\mu_B$ ,  $0.56\mu_B$ , and  $0.29\mu_B$  for the Co monomer, dimer, and trimer, respectively, as summarized in Fig. 7(e). Note that the magnetic moment of Co adatom on Cu(111) [57,58] is about  $2.0\mu_B$ , which is larger than the magnetic Co assembly on stanene/Cu(111), which could be related to the differences in atomic-scale orbital hybridization, bonding configuration, charge-density redistribution, and so on, in distinct systems. According to the PDOS in Fig. 7 and the STS measurements arranged in Fig. 6(e), the Co-atom assembly exhibits a peak feature at around  $-0.3$  eV in the  $dI/dU$  spectra, and we can further identify this peak coming from the maximum at  $-0.5$  eV of the Co-3d minority band, which is mainly contributed from the  $3d_{3z^2-r^2}$  orbital. We note that this conductance peak at  $-0.3$  eV has been reported on Co/Cu(111) [59], Co/Pt(111) [60], Co/Ir(111) [61], and Co/W(110) [62] in previous STS measurements. Despite a small deviation in energy position, this peak feature has been typically observed for the 2D Co nanoislands grown on a wide range of substrates. In combination of photoemission and DFT studies [60,62–66], the  $d$ -like minority character has been identified for this filled-state conductance peak.

As reported by Deng *et al.* [30], the ultraflat stanene on Cu(111) substrate has been characterized by the SOC-induced topological gap along with the inverted band structure and the helical edge states at the boundary. In addition, the bulk magnetic TIs that arose from the doping of magnetic atoms have been fabricated and exhibit a zero-field QAHE [32,36,51]. In the present work, by depositing the Co atoms onto the stanene/Cu(111) at 80 K, the self-assembled Co atomic structures, e.g., monomer, dimer, and trimer, have been fabricated. Note that the Co clusters with more random and complex geometries appear when the deposition amount of Co increases (see Fig. S4 of the Supplemental Material [56] for details). It is also noted that buckled honeycomb stanene can be grown on Cu(111) at 250 K [30] substrate temperature (see Fig. S5 of the Supplemental Material [56] for details).

Given the high spatial and energy resolution in the STS measurements, a characteristic peak feature at about  $-0.3$  eV has been resolved in  $dI/dU$  spectra at the Co atomic sites, which can be deduced from a maximum at around  $-0.5$  eV of the PDOS from the Co- $3d_{3z^2-r^2}$  minority band. As a result of the exchange-split Co-3d majority and minority bands, there are net magnetic moments of about  $0.60\mu_B$  in monomer,  $0.56\mu_B$  in dimer, and  $0.29\mu_B$  in trimer on the stanene/Cu(111). From the perspective of the doping stanene with Co impurities from our studies, such a magnetic Co assembly has provided a good starting point to develop atomic-scale magnetism in 2D stanene/Cu(111) with nontrivial topological properties. Note that we did not observe inelastic spin-flip excitations from these self-assembled Co atomic structures down to 4.2 K; one could try to perform the spectroscopic measurements at even lower temperature with improved energy resolution in the future.

#### IV. SUMMARY

In summary, self-assembled Co atomic structures have been fabricated on ultraflat stanene/Cu(111) by means of low-temperature growth. On account of atomically resolved topographic images and bias-dependent apparent heights, the Co monomer, dimer, and trimer structures from substituting Sn atoms have been deduced, which are in agreement with the self-consistent structural relaxations in DFT and have been further supported by STM simulations. In addition, the STS measurements with high spatial and energy resolution have resolved a conductance peak at about  $-0.3$  eV in the  $dI/dU$  spectra acquired at Co atomic sites, which can be explained by a maximum at around  $-0.5$  eV of the PDOS from the Co- $3d_{3z^2-r^2}$  minority band. Since there is an exchange splitting between the Co-3d majority and minority bands, nonzero magnetic moments have been found in the Co-atom assembly, ranging from about  $0.60\mu_B$  in monomer, to about  $0.56\mu_B$  in dimer, and to about  $0.29\mu_B$  in trimer on the stanene. These Co atomic structures, therefore, serve as the atomic-scale magnetic dopants, offering the quintessential spin ingredients to develop local magnetism in 2D topological nontrivial stanene.

#### ACKNOWLEDGMENTS

P.J.H. acknowledges support from C.-L. Hsieh for helium liquefier system operation in the instrumentation center of National Tsing Hua University under Grants No. MOST-110-2731-M-007-001 and No. MOST-111-2731-M-007-001, Ministry of Science and Technology of Taiwan under Grants No. MOST-111-2636-M-007-007 and No. MOST-110-2124-M-A49-008-MY3, and the center for quantum technology from the featured areas research center program within the framework of the higher education sprout project by the Ministry of Education (MOE) in Taiwan. J.H.T. acknowledges financial support from the Ministry of Science and Technology of Taiwan under Grants No. MOST-109-2112-M-007-034-MY3, and also from the NCHC, CINC-NTU, and AS-iMATE-109-13, Taiwan.

- [1] J. M. Kosterlitz and D. J. Thouless, *J. Phys. C* **5**, L124 (1972).
- [2] J. M. Kosterlitz and D. J. Thouless, *J. Phys. C* **6**, 1181 (1973).
- [3] M. Z. Hasan and C. L. Kane, *Rev. Mod. Phys.* **82**, 3045 (2010).
- [4] M. Z. Hasan and J. E. Moore, *Annu. Rev. Condens. Matter Phys.* **2**, 55 (2011).
- [5] X.-L. Qi and S.-C. Zhang, *Rev. Mod. Phys.* **83**, 1057 (2011).
- [6] K. V. Klitzing, G. Dorda, and M. Pepper, *Phys. Rev. Lett.* **45**, 494 (1980).
- [7] D. J. Thouless, M. Kohmoto, M. P. Nightingale, and M. den Nijs, *Phys. Rev. Lett.* **49**, 405 (1982).
- [8] C. L. Kane and E. J. Mele, *Phys. Rev. Lett.* **95**, 146802 (2005).
- [9] A. Kitaev, *Ann. Phys.* **303**, 2 (2003).
- [10] C. Nayak, S. H. Simon, A. Stern, M. Freedman, and S. Das Sarma, *Rev. Mod. Phys.* **80**, 1083 (2008).
- [11] A. Hirohata, K. Yamada, Y. Nakatani, I.-L. Prejbeanu, B. Diény, P. Pirro, and B. Hillebrands, *J. Magn. Magn. Mater.* **509**, 166711 (2020).
- [12] J. E. Moore, *Nature (London)* **464**, 194 (2010).
- [13] M. König, H. Buhmann, L. W. Molenkamp, T. Hughes, C.-X. Liu, X.-L. Qi, and S.-C. Zhang, *J. Phys. Soc. Jpn.* **77**, 031007 (2008).
- [14] L. Fu and C. L. Kane, *Phys. Rev. B* **76**, 045302 (2007).
- [15] X.-L. Qi and S.-C. Zhang, *Phys. Today* **63**, 33 (2010).
- [16] L. Fu, C. L. Kane, and E. J. Mele, *Phys. Rev. Lett.* **98**, 106803 (2007).
- [17] X. Chen, X.-C. Ma, K. He, J.-F. Jia, and Q.-K. Xue, *Adv. Mater.* **23**, 1162 (2011).
- [18] J. Zhang, C.-Z. Chang, Z. Zhang, J. Wen, X. Feng, K. Li, M. Liu, K. He, L. Wang, X. Chen, Q.-K. Xue, X. Ma, and Y. Wang, *Nat. Commun.* **2**, 574 (2011).
- [19] L. Kou, Y. Ma, Z. Sun, T. Heine, and C. Chen, *J. Phys. Chem. Lett.* **8**, 1905 (2017).
- [20] S. Murakami, *J. Phys.: Conf. Ser.* **302**, 012019 (2011).
- [21] R. B. Laughlin, *Phys. Rev. B* **23**, 5632 (1981).
- [22] L. Li, F. Yang, G. J. Ye, Z. Zhang, Z. Zhu, W. Lou, X. Zhou, L. Li, K. Watanabe, T. Taniguchi *et al.*, *Nat. Nanotechnol.* **11**, 593 (2016).
- [23] F. D. M. Haldane, *Phys. Rev. Lett.* **61**, 2015 (1988).
- [24] C. L. Kane and E. J. Mele, *Phys. Rev. Lett.* **95**, 226801 (2005).
- [25] B. A. Bernevig and S.-C. Zhang, *Phys. Rev. Lett.* **96**, 106802 (2006).
- [26] B. A. Bernevig, T. L. Hughes, and S.-C. Zhang, *Science* **314**, 1757 (2006).
- [27] M. König, S. Wiedmann, C. Brüne, A. Roth, H. Buhmann, L. W. Molenkamp, X.-L. Qi, and S.-C. Zhang, *Science* **318**, 766 (2007).
- [28] Y. Yao, F. Ye, X.-L. Qi, S.-C. Zhang, and Z. Fang, *Phys. Rev. B* **75**, 041401(R) (2007).
- [29] Y. Xu, B. Yan, H.-J. Zhang, J. Wang, G. Xu, P. Tang, W. Duan, and S.-C. Zhang, *Phys. Rev. Lett.* **111**, 136804 (2013).
- [30] J. Deng, B. Xia, X. Ma, H. Chen, H. Shan, X. Zhai, B. Li, A. Zhao, Y. Xu, W. Duan *et al.*, *Nat. Mater.* **17**, 1081 (2018).
- [31] C.-Z. Chang, J. Zhang, M. Liu, Z. Zhang, X. Feng, K. Li, L.-L. Wang, X. Chen, X. Dai, Z. Fang, X.-L. Qi, S.-C. Zhang, Y. Wang, K. He, X.-C. Ma, and Q.-K. Xue, *Adv. Mater.* **25**, 1065 (2013).
- [32] C.-Z. Chang, J. Zhang, X. Feng, J. Shen, Z. Zhang, M. Guo, K. Li, Y. Ou, P. Wei, L.-L. Wang, Z.-Q. Ji, Y. Feng, S. Ji, X. Chen, J. Jia, X. Dai, Z. Fang, S.-C. Zhang, K. He, Y. Wang *et al.*, *Science* **340**, 167 (2013).
- [33] C.-X. Liu, S.-C. Zhang, and X.-L. Qi, *Annu. Rev. Condens. Matter Phys.* **7**, 301 (2016).
- [34] K. He, Y. Wang, and Q.-K. Xue, *Natl. Sci. Rev.* **1**, 38 (2014).
- [35] C.-X. Liu, X.-L. Qi, X. Dai, Z. Fang, and S.-C. Zhang, *Phys. Rev. Lett.* **101**, 146802 (2008).
- [36] Y. Deng, Y. Yu, M. Z. Shi, Z. Guo, Z. Xu, J. Wang, X. H. Chen, and Y. Zhang, *Science* **367**, 895 (2020).
- [37] Z. Qiao, S. A. Yang, W. Feng, W.-K. Tse, J. Ding, Y. Yao, J. Wang, and Q. Niu, *Phys. Rev. B* **82**, 161414(R) (2010).
- [38] K. He, Y. Wang, and Q.-K. Xue, *Annu. Rev. Condens. Matter Phys.* **9**, 329 (2018).
- [39] J. Wang, B. Lian, and S.-C. Zhang, *Phys. Scr.* **2015**, 014003 (2015).
- [40] M. Nadeem, A. R. Hamilton, M. S. Fuhrer, and X. Wang, *Small* **16**, 1904322 (2020).
- [41] Y. L. Chen, J.-H. Chu, J. G. Analytis, Z. K. Liu, K. Igarashi, H.-H. Kuo, X. L. Qi, S. K. Mo, R. G. Moore, D. H. Lu, M. Hashimoto, T. Sasagawa, S. C. Zhang, I. R. Fisher, Z. Hussain, and Z. X. Shen, *Science* **329**, 659 (2010).
- [42] R. Yu, W. Zhang, H.-J. Zhang, S.-C. Zhang, X. Dai, and Z. Fang, *Science* **329**, 61 (2010).
- [43] C.-Z. Chang, W. Zhao, D. Y. Kim, H. Zhang, B. A. Assaf, D. Heiman, S.-C. Zhang, C. Liu, M. H. Chan, and J. S. Moodera, *Nat. Mater.* **14**, 473 (2015).
- [44] M. Li, C.-Z. Chang, L. Wu, J. Tao, W. Zhao, M. H. W. Chan, J. S. Moodera, J. Li, and Y. Zhu, *Phys. Rev. Lett.* **114**, 146802 (2015).
- [45] M. M. Otrokov, I. I. Klimovskikh, H. Bentmann, D. Estyunin, A. Zeugner, Z. S. Aliev, S. Gaß, A. Wolter, A. Koroleva, A. M. Shikin *et al.*, *Nature (London)* **576**, 416 (2019).
- [46] R. C. Vidal, A. Zeugner, J. I. Facio, R. Ray, M. H. Haghghi, A. U. B. Wolter, L. T. Corredor Bohorquez, F. Cagliaris, S. Moser, T. Figgemeier, T. R. F. Peixoto, H. B. Vasili, M. Valvidares, S. Jung, C. Cacho, A. Alfonsov, K. Mehlawat, V. Kataev, C. Hess, M. Richter, B. Büchner, J. van den Brink *et al.*, *Phys. Rev. X* **9**, 041065 (2019).
- [47] H. Zhang, C.-X. Liu, X.-L. Qi, X. Dai, Z. Fang, and S.-C. Zhang, *Nat. Phys.* **5**, 438 (2009).
- [48] Y. L. Chen, J. G. Analytis, J.-H. Chu, Z. K. Liu, S.-K. Mo, X. L. Qi, H. J. Zhang, D. H. Lu, X. Dai, Z. Fang, S. C. Zhang, I. R. Fisher, Z. Hussain, and Z.-X. Shen, *Science* **325**, 178 (2009).
- [49] Z. Liu, D. Qian, Y. Jiang, and J. Wang, [arXiv:2109.06178](https://arxiv.org/abs/2109.06178).
- [50] C. Liu, Y. Wang, H. Li, Y. Wu, Y. Li, J. Li, K. He, Y. Xu, J. Zhang, and Y. Wang, *Nat. Mater.* **19**, 522 (2020).
- [51] Y. Gong, J. Guo, J. Li, K. Zhu, M. Liao, X. Liu, Q. Zhang, L. Gu, L. Tang, X. Feng, D. Zhang, W. Li, C. Song, L. Wang, P. Yu, X. Chen, Y. Wang, H. Yao, W. Duan, Y. Xu *et al.*, *Chin. Phys. Lett.* **36**, 076801 (2019).
- [52] G. Kresse and J. Hafner, *Phys. Rev. B* **47**, 558 (1993).
- [53] G. Kresse and J. Furthmüller, *Comput. Mater. Sci.* **6**, 15 (1996).
- [54] G. Kresse and J. Furthmüller, *Phys. Rev. B* **54**, 11169 (1996).
- [55] G. Kresse and D. Joubert, *Phys. Rev. B* **59**, 1758 (1999).
- [56] See Supplemental Material at <http://link.aps.org/supplemental/10.1103/PhysRevMaterials.6.066001> for additional figures.
- [57] V. S. Stepanyuk, L. Niebergall, R. C. Longo, W. Hergert, and P. Bruno, *Phys. Rev. B* **70**, 075414 (2004).
- [58] M. Huang and S. Wu, *Vacuum* **197**, 110812 (2022).
- [59] O. Pietzsch, A. Kubetzka, M. Bode, and R. Wiesendanger, *Phys. Rev. Lett.* **92**, 057202 (2004).

- [60] F. Meier, K. von Bergmann, P. Ferriani, J. Wiebe, M. Bode, K. Hashimoto, S. Heinze, and R. Wiesendanger, *Phys. Rev. B* **74**, 195411 (2006).
- [61] J. E. Bickel, F. Meier, J. Brede, A. Kubetzka, K. von Bergmann, and R. Wiesendanger, *Phys. Rev. B* **84**, 054454 (2011).
- [62] J. Wiebe, L. Sacharow, A. Wachowiak, G. Bihlmayer, S. Heinze, S. Blügel, M. Morgenstern, and R. Wiesendanger, *Phys. Rev. B* **70**, 035404 (2004).
- [63] L. Diekhöner, M. A. Schneider, A. N. Baranov, V. S. Stepanyuk, P. Bruno, and K. Kern, *Phys. Rev. Lett.* **90**, 236801 (2003).
- [64] F. J. Himpsel and D. E. Eastman, *Phys. Rev. B* **20**, 3217 (1979).
- [65] H. Knoppe and E. Bauer, *Phys. Rev. B* **48**, 1794 (1993).
- [66] S. N. Okuno, T. Kishi, and K. Tanaka, *Phys. Rev. Lett.* **88**, 066803 (2002).